Soft-Lubrication Drainage and Rupture in Particle-Driven Vesicles

Yuan-Nan Young,[1,*] Bryan Quaife,[2] Herve Nganguia,[3] On Shun Pak,[4] Jie Feng,[5] and Howard A. Stone[6,†]
[1]Department of Mathematical Sciences, New Jersey Institute of Technology, Newark, New Jersey 07102, USA
[2]Department of Scientific Computing, Florida State University, Tallahassee, Florida 32306, USA
[3]Department of Mathematics, Towson University, Baltimore, Maryland 21252, USA
[4]Department of Mechanical Engineering, Santa Clara University, Santa Clara, California 95053, USA
[5]Department of Mechanical Sciences and Engineering, University of Illinois Urbana-Champaign, Urbana, Illinois 61801, USA
[6]Department of Mechanical and Aerospace Engineering, Princeton University, Princeton, New Jersey 08544, USA

(Received 30 October 2025; accepted 16 April 2026; published 20 May 2026)

The deformation and rupture of a lipid vesicle due to the forced normal approach of an inclusion are essential for optimizing the design of magnetic giant unilamellar vesicles (GUV) [Malik *et al.*, Nanoscale **17**, 13720 (2025)], with implications for active colloid-membrane interactions and cellular-scale chemical delivery. Here, we investigate vesicles propelled by a force-driven rigid inclusion and reveal a robust elastohydrodynamic mechanism: the inclusion outpaces the vesicle, sustaining a thinning film that drains symmetrically and self-similarly, largely independent of the initial shape. For soft membranes and small inclusions, the coupling drives a monotonic tension increase that can exceed the lysis tension. Evaluating the maximal tension over a delivery distance, we map an operating window in a vesicle reduced area and size relative to the inclusion.

DOI: 10.1103/1jsk-9q7w

Lipid vesicles encapsulating colloids or microswimmers provide an *in vitro* platform for active-membrane physics, with membrane-inclusion interactions setting the dynamics relevant to protocell evolution [1–4], pathogen motility [5], and targeted delivery [6,7]. Experiments with encapsulated *Bacillus subtilis* and active Janus particles reveal vigorous reshaping of vesicles without sustained directed motion [8,9], whereas vesicles enclosing *Escherichia coli* display persistent propulsion via mechanical coupling between the flagellar bundle and the membrane tethers, forming a rotating helical assembly that drives the vesicle [10]. Both theory and computation link swimmer-induced vesicle shape changes to its propulsion [11–23], underscoring that, whether actively or passively driven, propulsion is set by how forces and torques are transmitted through the *soft-lubrication* film that separates the inclusion from the membrane [24–29].

This soft-lubrication framework also underpins collisions between a rigid sphere and a fluid interface or a thick elastic plate in viscous media, and connects to Hertzian-type quasistatic impacts with elastic sheets [30–33], where a balance between elastic, viscous, and inertial dissipations yields similarity laws for the film thickness and pressure [34]. Classic work by Jones and Wilson [35] demonstrated self-similar thinning for a sphere settling toward a fluid-fluid interface, with scalings set by the ratio of external forcing to surface tension: near a rigid wall, tension dominates forcing, and an intervening thin liquid film drains exponentially, $h \sim e^{-t/\tau}$ (with τ a time constant [36]), while for a deformable interface of finite tension one finds $h \sim t^{-1/4}$ (weak forcing) and $h \sim t^{-1/2}$ (moderate forcing) [35].

We investigate soft-lubrication flow generated as a rigid inclusion approaches a vesicle modeled as an inextensible fluid membrane with spatially varying tension. Lubrication flows driven by tangential motion near compliant substrates are well documented [27,37], but we focus on the *normal* approach toward a membrane of constant bending rigidity and nonuniform tension, enforcing inextensibility. As in the confinement of a squirmer within a viscous drop [13], hydrodynamic coupling between a force-driven colloid and the membrane produces vesicle propulsion. Previous experiments (see Supplemental Material [38]) across colloid sizes and vesicle deformabilities—from a nearly rigid spherical vesicle [Fig. 1(a)(i)] to a deformable one [Fig. 1(a)(ii)]—show cotranslation of the inclusion and vesicle at nearly identical speeds with an accompanying steady vesicle shape [29]. Guided by these results, we focus on the soft-lubrication drainage of the interstitial film—a regime that is difficult to probe experimentally and challenging to simulate using generic stencil-based computational fluid dynamics or standard lattice-Boltzmann solvers.

We start from the incompressible Stokes equations for fluid at $\mathbf{x} \in \Omega = \Omega_e \cup \Omega_i$ (Fig. 1)

$$\nabla \cdot \boldsymbol{\tau} = -\nabla P + \mu \Delta \mathbf{u} = \mathbf{0}, \qquad \nabla \cdot \mathbf{u} = 0, \tag{1}$$

*Contact author: yyoung@njit.edu
†Contact author: has@princeton.edu

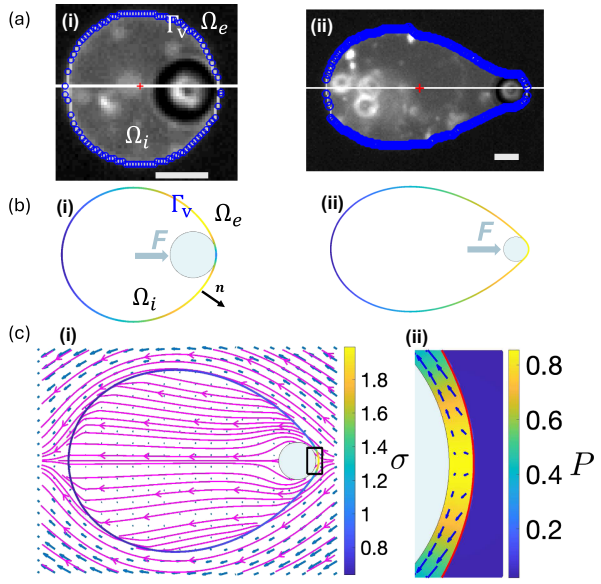

FIG. 1. Vesicle pushed by an inclusion particle under a constant force deforms and translates. (a) A magGUV under a constant, uniform magnetic field gradient. Scale bars are 5 μm. (b) Quasisteady simulated equilibrium shapes from 2D boundary-integral simulations: $(\bar{b}, \nu, \kappa_b) = (3, 0.99, 1)$ for (b)(i) and $(\bar{b}, \nu, \kappa_b) = (10, 0.9, 10^{-3})$ for (b)(ii). (c) The flow field around a vesicle pushed by a rigid inclusion (blue circle) in (b)(ii). The vesicle membrane is color-coded (i) by its tension σ, and the draining flow in the interstitial space is driven by the pressure gradient (ii).

where $\boldsymbol{\tau} = -P\boldsymbol{I} + \mu(\nabla\mathbf{u} + \nabla\mathbf{u}^T)$ is the stress tensor with pressure P, the incompressible flow field $\mathbf{u}$, and the fluid viscosity μ (assumed to be identical in both Ω_i and Ω_e). The jump in hydrodynamic traction across the vesicle membrane is balanced by the elastic membrane force density: $[\![\boldsymbol{\tau}]\!] \cdot \mathbf{n} = \mathbf{f}$ for $\mathbf{x} \in \Gamma_v$, where $[\![\cdot]\!]$ denotes the jump across Γ_v, $\mathbf{n}$ is the unit outward normal on Γ_v, and $\mathbf{f}$ is the membrane force density arising from bending elasticity and membrane tension. We use the magnitude of the external force per length (in 2D) $|\mathbf{F}|$ on the inclusion, the inclusion radius a_0, and viscosity μ to nondimensionalize the equations [38]. The vesicle-inclusion system is then parametrized by a dimensionless bending stiffness κ_b (membrane bending stiffness scaled to $|\mathbf{F}|a_0^2$), a size ratio $\bar{b} = \sqrt{A_0/(\pi a_0^2)}$, and membrane deformability, which in 2D can be characterized by the reduced area $\nu = 4\pi A_0/L_0^2$ with A_0 the enclosed area and L_0 the circumference of the membrane. We modified a fast, high-order 2D boundary-integral solver [44] to simulate the coupled fluid–membrane dynamics [38]. The method efficiently resolves the lubrication flow in the near-contact gap between the inclusion and membrane with high fidelity [Figs. 1(b) and 1(c)], and the scaling analysis below shows that the resulting similarity structure is identical between 2D and 3D axisymmetric geometries. By contrast, fully 3D axisymmetric simulations that resolve near-contact soft-lubrication are far more expensive: they require high-order surface discretizations, near-singular quadrature, and much smaller time steps [45]. An alternative based on the method of fundamental solutions can capture lubrication between nearly touching *rigid* surfaces [46], but it becomes severely ill conditioned as the gap closes and is inapplicable when one boundary is deformable.

Our 2D simulations at matched parameters (see discussions in Supplemental Material [38]) capture the trends in experimentally observed vesicle shape [Fig. 1(b)]. In the near-contact regime, lubrication pressures dominate, drive finite membrane deformations, and generate strong spatial tension σ gradients that regulate a nonlinear response [Figs. 1(c)(i) and 1(c)(ii)]. Within the interstitial film, the pressure peaks on the symmetry axis, regulating the drainage flow that controls the overall approach of the inclusion toward the membrane. Simulations show that, under constant forcing on the rigid inclusion, the vesicle translates at a speed U_v, computed as the average velocity of the membrane in the lab frame (see Supplemental Material [38]), and is slower than the inclusion lab-frame speed, U_p—even in near contact when the intervening lubrication film drains [Fig. 2(a)(i)]. From the initial configuration at $t = 0$ [Fig. 2(a)(ii)], the inclusion initially outruns the membrane, approaches near contact, and then (by $t = 400$) the pair cotranslate in a "quasisteady equilibrium," where the membrane and tension profiles in the near-contact region relax and stay approximately stationary compared to the slow drainage in the neck [Fig. 2(a)(iii)], where a nonuniform tension $\sigma(\theta, t)$ creates a Marangoni stress to compete with the pressure-driven flow in the thin film.

The same transient dynamics occurs for all initial conditions. For a spherical inclusion in experiments (3D) (circular inclusion in 2D simulations), the forcing direction [$\theta = 0$ in Fig. 2(a)(i)] sets the symmetry axis and the quasisteady equilibrium shape. Three robust morphologies emerge: (i) a *stiff* membrane with nearly uniform tension forms a locally quadratic film [Fig. 2(b)]; (ii) a *soft, less deformable* membrane produces a dimple with a pronounced tension peak at the symmetry axis [Fig. 2(c)]; and (iii) a *soft, more deformable* membrane develops a dimple with an extended neck and nearly uniform tension [Fig. 2(d)].

Once near-contact is reached, the subsequent dynamics are insensitive to the initial state: the external forcing sets the symmetry axis, the membrane relaxes to a quasisteady shape, and the lubrication layer thins monotonically. For an axisymmetric inclusion, the film profile $h(\theta, t)$ is a function of the polar angle θ [with the on-axis film thickness denoted by $h_0(t) \equiv h(\theta = 0, t)$]. The mass conservation of fluid in the interstitial space between an elastic, inextensible membrane and a normally approaching rigid inclusion yields the dimensionless lubrication equation

$$\partial_t h = \frac{1}{g(\theta)} \partial_\theta \left[g(\theta) \left(\frac{\epsilon^2}{3} (h^3 \partial_\theta P) - \frac{\epsilon}{2} (h^2 \partial_\theta \sigma) \right) \right], \quad (2)$$

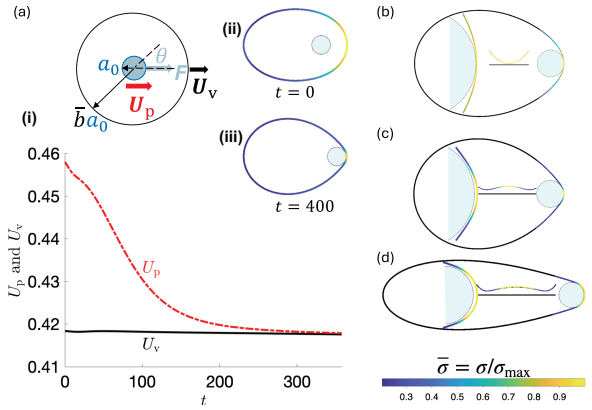

FIG. 2. Particle-vesicle dynamics. (a) Transient dynamics to the quasisteady equilibrium configurations, and (b)–(d) quasisteady equilibrium shapes color-coded by $\bar{\sigma} = \sigma/\sigma_{max}$ with $\bar{b} = 5$ and the black bars in the inset denoting the inclusion boundary (flattened for visualization). (a)(i) Particle speed U_p and vesicle speed U_v as a function of time. Schematic showing the polar angle θ with respect to the forcing direction. (a)(ii) and (a)(iii) Configurations at $t = 0$ and $t = 400$. (b) A stiff membrane ($\kappa_b = 1$ and $\nu = 0.95$) and a quadratic film profile in the inset. (c) A soft, less deformable membrane ($\kappa_b = 10^{-3}$ and $\nu = 0.95$) and a dimple-shaped film profile in the inset. (d) A soft, more deformable membrane ($\kappa_b = 10^{-3}$ and $\nu = 0.65$) and a dimple-shaped film profile in the inset.

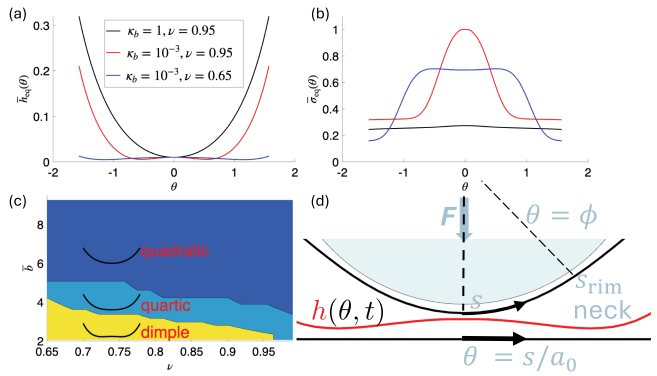

FIG. 3. Quasisteady thin film characteristics. (a) 2D quasisteady equilibrium film profiles, and (b) their corresponding tension distributions. $\bar{b} = 5$. Black curves: stiff vesicle; red curves: soft and less deformable vesicle; blue curves: soft and more deformable vesicle. (c) Distribution of equilibrium film profiles in size ratio $\bar{b}$ and reduced area ν for a stiff membrane ($\kappa_b = 1$). (d) Dimple-shaped film profile $h(\theta, t)$ with the angle $\theta = s/a_0$. The neck is located at the $\theta = \phi$. $(\bar{b}, \nu, \kappa_b) = (5, 0.95, 10^{-3})$.

where $\epsilon \ll 1$ is the aspect ratio of film height to particle radius, and $g(\theta) = 1$ and $g(\theta) = \sin\theta$ for 2D and 3D, respectively. The pressure P in the thin film depends on both the membrane shape (an elastic force proportional to κ_b) and the membrane tension σ determined from the area incompressibility. We provide a local analysis of Eq. (2) in the Supplemental Material [38] to illustrate the existence of both a quasisteady quadratic film profile and a dimple-shaped film profile.

First we focus on the quasisteady shapes ($\partial_t h \approx 0$). In 2D, three robust morphologies emerge, organized by the bending stiffness κ_b and reduced area ν. (i) For a *stiff, less-deformable* membrane ($\kappa_b \sim 1$, $\nu \approx 1$), the film is locally quadratic with nearly uniform tension [black; Figs. 3(a) and 3(b)]. (ii) For a *soft, less-deformable* membrane ($\kappa_b \ll 1$, $\nu \approx 1$), the profile is *dimpled* and the tension exhibits a sharp peak on the symmetry axis [red; Figs. 3(a) and 3(b)]. (iii) For a *soft, more-deformable* membrane ($\kappa_b \ll 1$, ν "significantly" smaller than unity), the dimple develops an *extended neck* with a broadly distributed tension across that region [blue; Figs. 3(a), 3(b), and 3(d)]. To fully determine the quasisteady profiles, the tension field required by local area incompressibility is obtained from the 2D simulations. For a stiff membrane with $\kappa_b = 1$, different quasisteady profiles are summarized in a morphology map in the $(\bar{b}, \nu)$ plane [Fig. 3(c)]; for a soft membrane with $\kappa_b = 10^{-3}$, the quasisteady film is dimpled within the explored range $\nu \in [0.65, 0.95]$.

Local analysis of the quasisteady equilibrium 3D axisymmetric thin film shows that the quadratic profile is possible only when the squeezing flow is between two rigid boundaries, such as a spherical inclusion against a spherical vesicle. Furthermore, we find that the thin-film profile between a rigid sphere squeezing against a deformable membrane is always dimple shaped, and the convexity depends on the Marangoni stress (see Supplemental Material [38]). The dimple-shaped thin-film profile in Fig. 3(a) is similar to the liquid film between an elastic sheet and a solid wall [47,48], between adhesive vesicles [49], and between viscous drops in squeeze-flow-like configurations under force [35,50,51] or shear [52,53], where soft-lubrication flow drives self-similar drainage.

Next we focus on the draining of a dimple-shaped film as a rigid inclusion approaches an elastic inextensible membrane. The drainage of a quadratic film profile is related to the thinning film between a rigid sphere and a rigid wall, where the self-similar scaling is significantly different between 2D and 3D [36]. Our matched asymptotic analysis of the inner region around the film neck [Fig. 3(d); see Supplemental Material] shows that the drainage scaling for the inner region of a dimple-shaped film is universal between 2D and 3D axisymmetric geometries [38]; we use our boundary-integral simulations to further uncover the universal self-similar scaling exponents that depend on both membrane stiffness (κ_b) and deformability (ν) as we elucidate below.

In particular, simulations of a rigid disk approaching a deformable, inextensible membrane reveal distinct drainage regimes [Figs. 4(a) and 4(b)]: the drainage follows $h_0(t) \sim t^{-\alpha}$ with α set by the bending stiffness κ_b and deformability ν. For a *stiff* membrane ($\kappa_b = 1$) we recover $\alpha \approx 2$, matching the rigid-wall limit of a cylinder

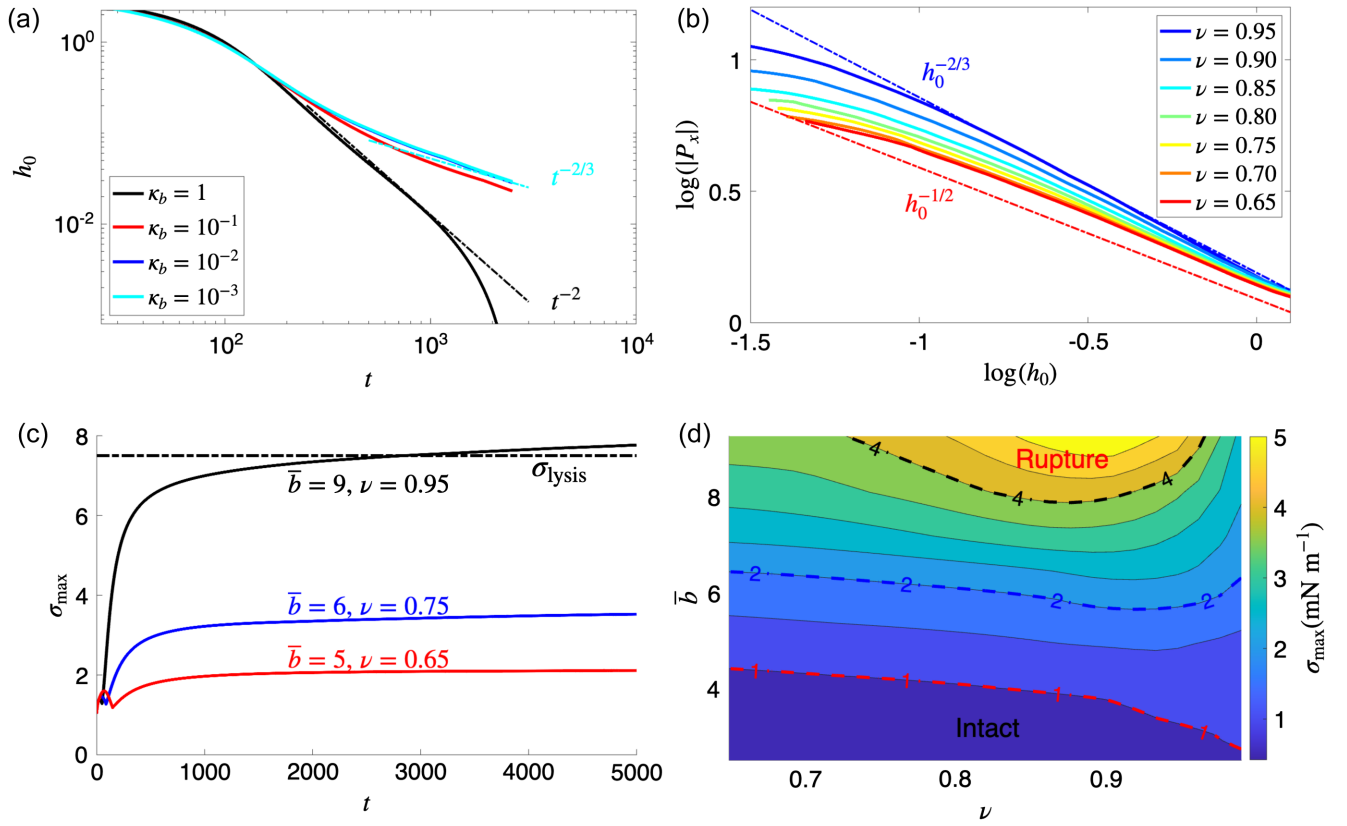

FIG. 4. Scaling of thin-film drainage from 2D simulations. $\bar{b} = 6$ for results in (a) and (b). (a) Neck drainage for $\nu = 0.95$: $h_0(t)$ decays self-similarly. (b) Pressure gradient-height scaling ($|P_x|$ vs h_0) for a soft membrane ($\kappa_b = 10^{-3}$) as deformability varies from $\nu = 0.95$ (blue) to $\nu = 0.65$ (red). (c) Maximum membrane tension $\sigma_{\max}$ for three pairs of size ratio $\bar{b}$ and ν at $\kappa_b = 10^{-3}$; dashed line: lysis tension σ_{lysis} scaled to $|\mathbf{F}| = 5 \times 10^{-4}$ N m^{-1}. (d) Map of dimensional $\sigma_{\max}$ (mN m^{-1}) over $(\nu, \bar{b})$. Rupture is predicted above the black contour, where the maximum membrane tension $\sigma_{\max}$ reaches the lysis threshold $\sigma_{\max} = \sigma_{\text{lysis}} \sim 4$ mN m^{-1} before the particle-vesicle travels 2 mm.

approaching a plane [36] across a range of values for $\nu \in [0.65, 0.99]$. For a *soft* membrane ($\kappa_b = 10^{-3}$) we numerically find $\alpha \approx 2/3$ over the same range of ν, larger than the fluid-interface case of a rigid sphere ($\alpha = 1/2$) [35], reflecting the finite bending resistance that shifts the dynamics toward the rigid-wall limit: $\alpha = 2$ in 2D [36]. Also the pressure gradient scales with the neck height as $|P_x| \sim h_0^{\beta}$, with β varying with deformability: $\beta \approx -2/3$ at $\nu = 0.95$ and $\beta \approx -1/2$ at $\nu = 0.65$, while the drainage exponent remains fixed at $\alpha \approx 2/3$ [Fig. 4(b)]. Under constant forcing, the drainage of a quadratic film profile is fixed by a single pair (α, β). By contrast, dimpled profiles exhibit nonunique β at the same α, indicating *two* tangential length scales—one governing pressure variation, the other advective outflow—consistent with the scaling analysis in Supplemental Material.

To understand such complex interplays between multiple scales in the drainage dynamics of a dimpled-shaped thin film, we focus on the drainage in the "inner" region where the film height is smallest at the dimple neck [35]. We introduce inner similarity variables along the membrane arclength s measured from the rim at $\theta = \phi$ [Fig. 3(d)]: $s - s_{\text{rim}}(t') = \ell(t')\xi$, $h(s, t') = H(t')J(\xi)$, $\sigma(s, t') = \sigma_0(t')G(\xi, t')$, with general power-law scalings in term of the amplitude $j = j(t')$ that encode the self-similar behavior: $H = j^{2\hat{\alpha}}$, $\ell = \hat{\beta} j^{\hat{\lambda}}$, $\sigma_0 = j^{\hat{c}_0}$, $G = j^{\hat{c}_1}\tilde{G}(\xi)$. Here t' is the characteristic time for inner scaling [35], and $J(\xi)$ and $\tilde{G}(\xi)$ are order-one similarity shapes. The equation for the depth-averaged interfacial flux, under small-slope linearization (capillarity and bending) in the inner region of Eq. (2), is

$$\partial_\xi^3 J - \frac{\kappa_b}{\hat{\beta}^2} j^{-(2\hat{\lambda}+\hat{c}_0)} \partial_\xi^5 J - \frac{3\hat{\beta}^2}{2J} j^{2\hat{\lambda}-4\hat{\alpha}+\hat{c}_1} \partial_\xi \tilde{G} = \mathcal{F} \frac{dj}{dt'}, \quad (3)$$

where $\mathcal{F} = j^{3\hat{\lambda}-8\hat{\alpha}}/(g(\phi)J^3)$, with $g(\phi) = 1(\sin\phi)$ for the 2D cylinder (3D axisymmetric) geometry. To leading order, the 2D and 3D problems share the *same* similarity operator and exponents. Therefore, the drainage scaling in the 2D simulations shed light on the self-similar draining dynamics that is especially challenging to study in 3D axisymmetric boundary-integral simulations.

Next, for self-similar drainage, we require the powers of $j(t')$ multiplying the operator terms in Eq. (3) to vanish for an ordinary differential equation in ξ only on the left-hand side. This yields the separation conditions,

$$2\hat{\lambda} + \hat{c}_0 = 0 \quad \text{and} \quad 2\hat{\lambda} - 4\hat{\alpha} + \hat{c}_1 = 0. \tag{4}$$

We then combine Eq. (4) with the numerically determined scaling in Figs. 4(a) and 4(b), for the height decay and for the pressure-gradient (tension-gradient) scalings, to solve for $(\hat{\alpha}, \hat{\lambda}, \hat{c}_0, \hat{c}_1)$ for two reduced areas: $\nu = 0.65$ [red solid curve in Fig. 4(b), highly deformable] and $\nu = 0.95$ [blue solid curve in Fig. 4(b), less deformable]. For $\nu = 0.65$, the drainage scaling in Fig. 4(a) and the gradient scaling in Fig. 4(b) are

$$\frac{2\hat{\alpha}}{3\hat{\lambda} - 8\hat{\alpha} + 1} = -\frac{2}{3}, \qquad \frac{\hat{c}_0 + \hat{c}_1 - \hat{\lambda}}{2\hat{\alpha}} = -\frac{1}{2}. \tag{5}$$

Together with Eq. (4) we obtain $\hat{\alpha} = \hat{\lambda} = 1/2$ and $\hat{c}_0 = -\hat{c}_1 = -1$. Hence the membrane tension scales as $\sigma \sim \sigma_0 G \sim j^{\hat{c}_0+\hat{c}_1} \sim H^{(\hat{c}_0+\hat{c}_1)/(2\hat{\alpha})} = H^0$: it asymptotes to a constant during drainage when the membrane is soft and highly deformable [red and blue curves in Fig. 4(c)]. For $\nu = 0.95$, the drainage and gradient scalings imply

$$\frac{2\hat{\alpha}}{3\hat{\lambda} - 8\hat{\alpha} + 1} = -\frac{2}{3}, \qquad \frac{\hat{c}_0 + \hat{c}_1 - \hat{\lambda}}{2\hat{\alpha}} = -\frac{2}{3}, \tag{6}$$

which corresponds to $\hat{\alpha} = 5/9$, $\hat{\lambda} = 16/27$, $\hat{c}_0 = -32/27$, and $\hat{c}_1 = 28/27$. Therefore $(\hat{c}_0 + \hat{c}_1)/(2\hat{\alpha}) = -2/15$ and $\sigma \sim H^{-2/15} \sim t^{4/45}$, indicating a weak divergence of tension (and a long time to reach lysis threshold [38]) as the film drains when the membrane is soft but less deformable [black solid curve in Fig. 4(c)].

In Malik *et al.* [29], the vesicle-inclusion compound particle remains intact during transport, and ruptures only upon photoactivation at the target: GUV that encloses magnetic particles with an inclusion radius $a_0 = 3$ μm at a speed of $\sim 20\ \mu\mathrm{m\,s^{-1}}$ can travel for ~100 s (inside the visualization window) without rupture. This is consistent with our soft-lubrication analysis: as the inclusion approaches, the membrane tension increases while the minimal gap drains self-similarly. It also identifies a limitation—under sustained drive the tension can exceed the lysis tension (between 3 to 4 $\mathrm{mN\,m^{-1}}$ for a GUV under slow loading [54]) before arrival at the end of the visualization window. Using a 2 mm travel distance as a benchmark, boundary-integral simulations with $(\bar{b}, a_0) = (5\text{–}6, 3\ \mu\mathrm{m})$ and $|\mathbf{F}| \sim 10^{-8}\ \mathrm{N\,m^{-1}}$ ($|\mathbf{F}|a_0^2 = 10^{-19}$ J) keep peak tension below lysis [blue and red curves in Fig. 4(c)], whereas $(\bar{b}, a_0) = (9, 1.5\ \mu\mathrm{m})$ and $|\mathbf{F}| \sim 6 \times 10^{-5}\ \mathrm{N\,m^{-1}}$ ($|\mathbf{F}|a_0^2 = 10^{-16}$ J) exceed the lysis tension before 2 mm (black curve). Figure 4(d) maps the maximum vesicle tension attained over the travel distance in the $(\nu, \bar{b})$ plane, delineating rupture regions that we expect to be universal for both 2D and axisymmetric 3D vesicle membranes while $h_0 \gtrsim 15$ nm, a conservative estimate for the crossover length below which the finite membrane thickness must be taken into account [55,56]. The predicted rupture boundary is an order-of-magnitude guide, reflecting uncertainties in lysis tension, loading rates, and near-contact interactions.

In this work we analyzed the elastohydrodynamics of a rigid inclusion driven toward a deformable vesicle and showed that membrane bending and inextensibility organize the soft-lubrication flow into a robust similarity regime with universal scaling exponents bridging 2D and axisymmetric 3D configurations. The inclusion persistently outpaces the vesicle, the interstitial film drains self-similarly ($h_0 \sim t^{-2/3}$ for soft membranes), and the membrane tension rises monotonically, approaching a plateau for highly deformable vesicles or increasing slowly beyond lysis for stiffer ones. These results provide a quantitative framework for predicting the soft-lubrication flow and the onset of membrane rupture before molecular-scale effects, such as roughness, short-range adhesion or repulsion, and finite-thickness effects, dominate the drainage dynamics. The neck [Fig. 3(d)] plays a role analogous to the apparent contact radius in elastohydrodynamic adhesion, with the coupled balance of viscous drainage, Helfrich bending, and inextensible tension selecting the thin-film profile and its scaling. Together, these results identify a membrane-elastohydrodynamic mechanism that provides a direct handle to suppress premature rupture or enable on-demand release.

Acknowledgments—We thank Vinit Kumar Malik for helpful discussions. Y. N. Y. acknowledges support from NSF (DMS-1951600 and DMS-2510714) and Flatiron Institute, part of Simons Foundation. B. Q. acknowledges support from NSF (DMS-2510713). H. N. acknowledges support from NSF (DMS-2211633). O. S. P. acknowledges partial support from NSF (CBET-2323046 and CBET-2419945). J. F. acknowledges partial support from NSF (CBET-2323045). H. A. S. acknowledges support from NSF (CBET-224679).

Data availability—The data that support the findings of this article are openly available [38].

[1] J. C. Blain and J. W. Szostak, Annu. Rev. Biochem. **83**, 615 (2014).
[2] D. Babu, N. Katsonis, F. Lancia, R. Plamont, and A. Ryabchun, Nat. Rev. Chem. **6**, 377 (2022).
[3] Y. Miele, G. Holló, I. Lagzi, and F. Rossi, Life **12**, 841 (2022).
[4] Y. Minagawa, M. Yabuta, M. Su'etsugu, and H. Noji, Nat. Commun. **16**, 1522 (2025).
[5] P. Iyer, G. Gompper, and D. A. Fedosov, Soft Matter **18**, 6868 (2022).

[6] U. Bulbake, S. Doppalapudi, N. Kommineni, and W. Khan, Pharmaceutics **9**, 12 (2017).
[7] P. Liu, G. Chen, and J. Zhang, Molecules **27**, 1372 (2022).
[8] S. C. Takatori and A. Sahu, Phys. Rev. Lett. **124**, 158102 (2020).
[9] V. Willems, A. Baron, D. Fernandez-Matoz, G. Wolfisberg, J.-C. Baret, E. Dufresne, and L. Alvarez, Soft Matter **21**, 6175 (2025).
[10] L. L. Nagard, A. T. Brown, A. Dawson, V. A. Martinez, W. C. K. Poon, and M. Staykova, Proc. Natl. Acad. Sci. U.S.A. **119**, e2206096119 (2022).
[11] M. Paoluzzi, R. D. Leonardo, M. C. Marchetti, and L. Angelani, Sci. Rep. **6**, 1 (2016).
[12] J. Chen, Y. Hua, Y. Jiang, X. Zhou, and L. Zhang, Sci. Rep. **7**, 15006 (2017).
[13] S. Y. Reigh, L. Zhu, F. Gallaire, and E. Lauga, Soft Matter **13**, 3161 (2017).
[14] A. Daddi-Moussa-Ider, S. Goh, B. Liebchen, C. Hoell, A. J. T. M. Mathijssen, F. Guzmán-Lastra, C. Scholz, A. M. Menzel, and H. Löwen, J. Chem. Phys. **150**, 064906 (2019).
[15] C. Wang, Y.-k. Guo, W.-d. Tian, and K. Chen, J. Chem. Phys. **150**, 044907 (2019).
[16] W.-j. Shan, F. Zhang, W.-d. Tian, and K. Chen, Soft Matter **15**, 4761 (2019).
[17] A. R. Sprenger, V. A. Shaik, A. M. Ardekani, M. Lisicki, A. J. Mathijssen, F. Guzmán-Lastra, H. Löwen, A. M. Menzel, and A. Daddi-Moussa-Ider, Eur. Phys. J. E **43**, 58 (2020).
[18] H. R. Vutukuri, M. Hoore, C. Abaurrea-Velasco, L. van Buren, A. Dutto, T. Auth, D. A. Fedosov, G. Gompper, and J. Vermant, Nature (London) **586**, 52 (2020).
[19] Y.-N. Young, M. Shelley, and D. Stein, Math. Biosci. Eng. **18**, 2849 (2021).
[20] L. J. Ruske and J. M. Yeomans, Phys. Rev. X **11**, 021001 (2021).
[21] K. J. Marshall and J. F. Brady, J. Fluid Mech. **919**, A31 (2021).
[22] R. Kree and A. Zippelius, The Eur. Phys. J. E **44**, 6 (2021).
[23] P. Iyer, G. Gompper, and D. A. Fedosov, Soft Matter **19**, 3436 (2023).
[24] K. Xiao, R. Ma, and C.-X. Wu, Phys. Rev. E **106**, 044411 (2022).
[25] J. M. Skotheim and L. Mahadevan, Phys. Rev. Lett. **92**, 245509 (2004).
[26] V. Bertin, Y. Amarouchene, E. Raphaël, and T. Salez, J. Fluid Mech. **933**, A23 (2022).
[27] B. Rallabandi, Annu. Rev. Fluid Mech. **56**, 491 (2024).
[28] F. Fessler, P. Muller, and A. Stocco, arXiv:2503.17465.
[29] V. K. Malik, C.-T. Liao, C. Xu, A. Daddi-Moussa-Ider, O. S. Pak, Y.-N. Young, and J. Feng, Nanoscale **17**, 13720 (2025).
[30] A. Gopinath and L. Mahadevan, Proc. R. Soc. A **467**, 1665 (2011).
[31] B. Rallabandi, N. Oppenheimer, M. Y. B. Zion, and H. A. Stone, Nat. Phys. **14**, 1211 (2018).
[32] A. Daddi-Moussa-Ider, B. Rallabandi, S. Gekle, and H. A. Stone, Phys. Rev. Fluids **3**, 084101 (2018).
[33] A. Farutin, arXiv:2508.00080.
[34] J. H. Snoeijer, J. Eggers, and C. H. Venner, Phys. Fluids **25**, 101705 (2013).
[35] A. Jones and S. Wilson, J. Fluid Mech. **87**, 263 (1978).
[36] H. A. Stone, Chem. Eng. Sci. **60**, 4838 (2005).
[37] L. Bureau, G. Coupier, and T. Salez, Eur. Phys. J. E **46**, 111 (2023).
[38] See Supplemental Material at http://link.aps.org/supplemental/10.1103/1jsk-9q7w for brief description, which includes Refs. [39–43].
[39] Akanksha Moga, Naresh Yandrapalli, Rumiana Dimova, and Tom Robinson, Chembiochem **20**, 2674 (2019).
[40] Olga Baun and Peter Blümler, J. Magn. Magn. Mater. **439**, 294 (2017).
[41] Gábor Holló, Ylenia Miele, Federico Rossi, and István Lagzi, Phys. Chem. Chem. Phys. **23**, 4262 (2021).
[42] Giovanni Ghigliotti, Thierry Biben, and Chaouqi Misbah, J. Fluid Mech. **653**, 489 (2010).
[43] J F Brady and G Bossis, J. Fluid Mech. **155**, 105 (1985).
[44] B. Quaife and G. Biros, J. Comput. Phys. **274**, 245 (2014).
[45] S. K. Veerapaneni, D. Gueyffier, G. Biros, and D. Zorin, J. Comput. Phys. **228**, 7233 (2009).
[46] A. Broms, A. H. Barnett, and A.-K. Tornberg, J. Comput. Phys. **523**, 113636 (2025).
[47] Y.-N. Young, S. Veerapaneni, and M. J. Miksis, J. Fluid Mech. **751**, 406 (2014).
[48] Y.-N. Young and H. A. Stone, Phys. Rev. Fluids **2**, 064001 (2017).
[49] B. Quaife, S. Veerapaneni, and Y.-N. Young, Phys. Rev. Fluids **4**, 103601 (2019).
[50] T. Bai, R. Manica, B. Liu, E. Klaseboer, Z. Xu, and Q. Liu, Phys. Rev. Lett. **127**, 124503 (2021).
[51] L. Duchemin and C. Josserand, Proc. Natl. Acad. Sci. U.S.A. **117**, 20416 (2020).
[52] R. Tsekov and E. Ruckenstein, Colloids Surf. A **82**, 255 (1994).
[53] J. Lowengrub, J. Allard, and S. Aland, J. Comput. Phys. **309**, 112 (2016).
[54] T. Portet and R. Dimova, Biophys. J. **99**, 3264 (2010).
[55] U. Seifert and S. A. Langer, Europhys. Lett. **23**, 71 (1993).
[56] Z. G. Lipel, Yannick A. Omar, and D. Fraggedakis, Phys. Rev. Fluids **10**, 103101 (2025).